






RESEARCH ARTICLE | JANUARY 05 2022

## Dynamics of droplet impact on a ring surface

Chensen Lin (林晨森) ; Damin Cao (曹达敏); Dongxiao Zhao (赵东晓) ; Ping Wei (韦萍) ;  
Shuo Chen (陈硕)  ; Yang Liu (刘扬)



*Physics of Fluids* 34, 012004 (2022)

<https://doi.org/10.1063/5.0074977>



### Articles You May Be Interested In

A review of many-body dissipative particle dynamics (MDPD): Theoretical models and its applications

*Physics of Fluids* (November 2021)

Transverse effect on liquid viscosity: A many-body dissipative particle dynamics simulation study

*Physics of Fluids* (January 2022)

Influence of thermal fluctuations on nanoscale free-surface flows: A many-body dissipative particle dynamics study

*Physics of Fluids* (November 2021)



Physics of Fluids

Special Topics Open  
for Submissions

[Learn More](#)

# Dynamics of droplet impact on a ring surface

Cite as: Phys. Fluids **34**, 012004 (2022); doi: [10.1063/5.0074977](https://doi.org/10.1063/5.0074977)

Submitted: 12 October 2021 · Accepted: 17 December 2021 ·

Published Online: 5 January 2022



View Online



Export Citation



CrossMark

Chensen Lin (林晨森),<sup>1</sup> Damin Cao (曹达敏),<sup>1, 2</sup> Dongxiao Zhao (赵东晓),<sup>3</sup> Ping Wei (韦萍),<sup>1</sup>   
Shuo Chen (陈硕),<sup>1, a)</sup> and Yang Liu (刘扬)<sup>4</sup>

## AFFILIATIONS

<sup>1</sup>School of Aerospace Engineering and Applied Mechanics, Tongji University, Shanghai 200092, China

<sup>2</sup>School of Air Transportation, Shanghai University of Engineering Science, Shanghai 201620, China

<sup>3</sup>UM-SJTU Joint Institute, Shanghai Jiao Tong University, Shanghai 200240, China

<sup>4</sup>Department of Mechanical Engineering, The Hong Kong Polytechnic University, Hong Kong, China

<sup>a)</sup> Author to whom correspondence should be addressed: [schen\\_tju@tongji.edu.cn](mailto:schen_tju@tongji.edu.cn)

## ABSTRACT

We investigate the dynamics of droplet impacts on a ring-decorated solid surface, which is reported to reduce the integral of contact area over contact time by up to 80%. By using many-body dissipative particle dynamics (MDPD), a particle-based simulation method, we measure the temporal evolution of the shape and the impact force of two specific types of phenomena, overrun and ejection. The numerical model is first validated with experimental data on a plain surface from literature. Then, it is used to extract the impacting force of the ring and substrate separately, showing the ring does not provide the majority of vertical force to redirect the horizontal spreading. The impacting pressure in different concentric rings is also present as a function of time, showing pressure waves traveling from ring to center. The effect of the ring's height and radius on the impacting force is also discussed. To the best of our knowledge, this is the first MDPD study on droplets impacting on a solid surface with a validated force analysis.

Published under an exclusive license by AIP Publishing. <https://doi.org/10.1063/5.0074977>

## I. INTRODUCTION

Droplets impacting a surface are found in a variety of both natural and industrial phenomena. For example, in nature, droplet impacts can erode soil,<sup>1</sup> disrupt mosquito flight,<sup>2</sup> and even lead damaged leaf to early abscission.<sup>3</sup> In industrial applications, it is related to inkjet printing,<sup>4</sup> thermal or agricultural sprays,<sup>5</sup> erosion of steam or wind turbine blades,<sup>6</sup> and scouring aircraft.<sup>7</sup>

In each case, the force evolution associated with the droplet impact is highly important since it characterizes the time duration and the impulse. Furthermore, the force–time profile is essential to characterize material erosion in designing material processing applications since it provides an evolution of the time-dependent loading. This allows the calculation of stresses and strains experienced by the solid.

Many experimental studies<sup>8–11</sup> have investigated various aspects of the normal impingement of a liquid droplet onto a plain surface. The measurements reveal that the impact force is characterized by a rapid rise to a maximum, followed by a gradual decay to zero. Li *et al.*<sup>8</sup> found that the total time when a droplet imparts a normal force decreases with the impact velocity and increases with the increased droplet diameter. Zhang *et al.*<sup>9</sup> showed that the force–time profile is Reynolds number ( $Re = \rho U_0 D / \mu$ ) invariant above 230, where  $\rho$ ,  $U_0$ ,

$D$ , and  $\mu$  denote the liquid density, impact velocity, droplet diameter, and liquid viscosity. Conversely, viscosity plays a more dominant role as the  $Re$  decreases below 230, with the normalized peak force increasing and the normalized time duration decreasing.

More quantitatively, Philippi *et al.*<sup>12</sup> theoretically determined that during the initial pre-peak rise in force, the velocity and pressure fields adhere to a self-similar form and the normal impact force follows a  $\sqrt{t}$ -growth in time. This  $\sqrt{t}$ -force dependence is later verified by Gordillo *et al.*,<sup>10</sup> who has done a large number of experiments with a wide range of  $Re$ . However, the equations from Philippi *et al.*<sup>12</sup> or Gordillo *et al.*<sup>10</sup> all diverge from the measurements after the peak force; thus, they are only applicable at early times (dimensionless time  $\hat{t} = tU_0/D < 0.05$ ). However, considering the early-time force evolution has credible establishment both theoretically and experimentally, it is useful for validating new computational methods or new measurement tools.

After the peak force, a subsequent pressure decay begins. The exponential form of  $e^{-t}$  is used and discussed by many studies.<sup>13,14</sup> Although theoretical support is needed for the exponential decay, the use of  $e^{-t}$  to describe the post-peak decay observed in experiments is quite effective. Building on the previous work of the initial impact

model and post-peak model, Mitchell *et al.*<sup>11</sup> constructed a single model equation that accurately incorporates the early-time  $\sqrt{t}$ -force dependence and the post-peak  $e^{-t}$  decay across a wide range of  $Re$  and Weber numbers ( $We = \rho U_0^2 D / \sigma$ , where  $\sigma$  denotes the surface tension). This unified dimensionless model provides a useful contribution to applications, as well as validating new computational models.

For experimental research, which is the main approach in studying the impacting force evolution, the piezoelectric force sensor is widely used to measure the normal force.<sup>9,15,16</sup> A drawback of piezoelectric force sensors is the resonant ringing. Even though they have a high natural frequency ( $\sim 50$  kHz), they present strong resonant ringing since the interested time span is one or two milliseconds, which is not far from the natural frequency. One common method is applying the filter to obtain a smooth curve. However, the filter has many disadvantages, for example, the sharp increase is smoothed, or the whole signal is shifted.<sup>17</sup> Gordillo *et al.*<sup>10</sup> tackled this problem by targeting the impinging drops slightly off the center of the force sensor, which can reduce resonant ringing to some degree. Another drawback of piezoelectric force sensors is the dipolar interactions between droplets and the piezoelectric sensors, which infect the measured impacting normal force.<sup>10</sup> To minimize the effect, non-polar liquids like silicone oils must be used.

These drawbacks are opportunities for computational simulations. In addition to the absence of natural frequency when measuring, the sampling frequency can also be higher without cost. Moreover, the observation can be made from any angle, free from tight space or obstacles. For force measurement, the piezoelectric force sensors can only measure the impacting force on solid as a whole, while in simulation, the force can be measured in different user-defined regions. For example, we could analyze the distribution of forces along the radial distance by defining concentric rings. Furthermore, if the solid surface is geometrically heterogeneous, the force on different components can be measured separately. The flexibility of measurement makes the computational approach have exclusive advantages. However, the simulation results may deviate from the ground truth due to many reasons, such as the different prerequisites of computational models or different problem setups. In order to obtain credible results, the computational model must be validated with widely recognized experimental results or analytical results.

Many computational methods have been applied in the literature to droplet impacting problems, for example, computational fluid mechanics,<sup>18</sup> lattice Boltzmann methods,<sup>19</sup> and dissipative particle dynamics (DPD).<sup>20,21</sup> DPD is a mesoscale particle-based method, and it has been widely used in problems like red blood cells,<sup>22–24</sup> droplets or bubbles,<sup>25,26</sup> polymer,<sup>27,28</sup> and colloids.<sup>29</sup> There is also some pioneering work integrating machine learning technique with the DPD simulations.<sup>26,30</sup>

DPD has approached the droplet problem from many aspects,<sup>31–34</sup> but mainly from a morphology aspect. Among all the reported features, the impact force of liquid droplets leads to arguably the most important consequence of impact events. However, to the best of our knowledge, no previous DPD studies have measured the impacting force between solid and liquid. As a computational method, the force in DPD simulation is worth validating before further analysis. In this paper, we will compare the force in DPD simulation with experimental data, thus bridging up the gap in this field.

Among all kinds of surfaces, the plain surface is fundamental, and a droplet impacting on the plain surface has been studied the most thoroughly. A large number of studies can be found approaching this problem from different aspects under various conditions.<sup>35,36</sup> In the last decade, patterned surfaces have attracted much attention. These geometrically modified surfaces have proven to cause different dynamics when droplets impact on them, which could be useful in various applications. For example, Girard *et al.*<sup>37</sup> reported that a superhydrophobic surface decorated with a ring structure could redirect the spreading droplet into the air, thus reducing the interaction parameter up to 80%. The interaction parameter is defined as the integral of the liquid–solid contact area over time. It is more objective to use the interaction parameter rather than the contact time as criteria if our goal is to reduce or enhance the heat transfer between solid and droplets. They also reported two specific droplet phenomena after impacting on the ring, namely, overrun and ejection. In overrun, the spreading droplet would overrun the ring and continue spreading along the plain surface, while in ejection, the spreading liquid is redirected to the air and forming a waterbowl, and none of the solid outside the ring is wetted. As the ring radius increases, the shape evolution transits from overrun to ejection, and the interaction parameter associated with it drops sharply. Lin *et al.*<sup>38</sup> showed similar findings on the crater-like surface, which is a plain surface subtracted by a spherical cap. The measured interaction parameter can be reduced up to 75%. The authors also investigated the off-center impacting and the crater arrays to prove the effectiveness of this design. The ring surface, along with the crater-like surface, is promising in reducing the contact time and area; however, this direction is still in the early stage of exploration. Many aspects, such as the role of the ring in reducing the interaction parameter and the cause of overrun and ejection, need more insight. The previous studies mainly approach this problem from the aspects of contact parameter and the droplet morphology, hardly from the force aspect.

In this paper, we investigate the dynamics of a droplet impacting on the ring surface. First, we introduce the DPD method and the setup for the system in Sec. II. Specially, we tweak the DPD model a little for the problem. Then, in Sec. III, we validate the temporal force evolution on the plain surface with experimental and theoretical results from literature, and explore different aspects of the dynamics of droplets impacting on ring surface, including the force profiles of overrun and ejection, the pressure evolution along the horizontal radial direction, and the role of the ring. Finally, we end the paper with a summary in Sec. IV.

## II. METHODS AND MODEL CONFIGURATIONS

### A. Methods

A particle-based simulation method DPD is used in this study.<sup>39</sup> Similar to a molecular dynamics system, a DPD model consists of many interacting particles governed by Newton's equation of motion,<sup>40</sup>

$$m_i \frac{d^2 \mathbf{r}_i}{dt^2} = m_i \frac{d\mathbf{v}_i}{dt} = \mathbf{F}_i = \sum_{j \neq i} (\mathbf{F}_{ij}^C + \mathbf{F}_{ij}^D + \mathbf{F}_{ij}^R), \quad (1)$$

where  $m_i$  is the mass of the particle  $i$ ,  $\mathbf{r}_i$  and  $\mathbf{v}_i$  are the position and velocity vectors of the particle  $i$ , and  $\mathbf{F}_i$  is the total force acting on the particle  $i$  due to the presence of neighboring particles. The summation

for computing  $\mathbf{F}_i$  is carried out over all neighboring particles within a cutoff range. Beyond the cutoff, all pairwise interactions are considered zero. The pairwise force is comprised of a conservative force  $\mathbf{F}_{ij}^C$ , a dissipative force  $\mathbf{F}_{ij}^D$ , and a random force  $\mathbf{F}_{ij}^R$ , which, respectively, are of the form

$$\mathbf{F}_{ij}^C = a_{ij}\omega_C(r_{ij})\mathbf{e}_{ij}, \quad (2)$$

$$\mathbf{F}_{ij}^D = -\gamma_{ij}\omega_D(r_{ij})(\mathbf{v}_{ij}\mathbf{e}_{ij})\mathbf{e}_{ij}, \quad (3)$$

$$\mathbf{F}_{ij}^R \cdot d\mathbf{t} = \sigma_{ij}\omega_R(r_{ij})d\tilde{W}_{ij}\mathbf{e}_{ij}, \quad (4)$$

where  $r_{ij} = |\mathbf{r}_{ij}| = |\mathbf{r}_i - \mathbf{r}_j|$  is the distance between particles  $i$  and  $j$ ,  $\mathbf{e}_{ij} = \mathbf{r}_{ij}/r_{ij}$  is the unit vector,  $\mathbf{v}_{ij} = \mathbf{v}_i - \mathbf{v}_j$  is the velocity difference, and  $d\tilde{W}_{ij}$  is an independent increment of the Wiener process.<sup>41</sup> The coefficients  $a_{ij}$ ,  $\gamma_{ij}$ , and  $\sigma_{ij}$  determine the strength of the three forces, respectively. To satisfy the fluctuation-dissipation theorem<sup>41</sup> and to maintain the DPD system at a constant temperature  $T$ , the dissipative force and the random force are constrained by  $\sigma_{ij}^2 = 2\gamma_{ij}k_B T$  and  $\omega_D(r_{ij}) = \omega_R^2(r_{ij})$ , where  $k_B$  is the Boltzmann's constant. Common choices for weight functions are  $\omega_C(r_{ij}) = 1 - r_{ij}/r_c$ ,  $\omega_D(r_{ij}) = \omega_R^2(r_{ij}) = (1 - r_{ij}/r_c)^{1/2}$  with  $r_c$  being the cutoff radius.

With the purely repulsive conservative forces, DPD cannot achieve the vapor–liquid coexistence. To break this limitation, Warren<sup>42</sup> modified the conservative force term to include an attractive force and established the many-body dissipative particle dynamics (MDPD). The repulsive force of MDPD depends on a weighted average of the local density, whereas the attractive force is density independent,

$$\mathbf{F}_{ij}^C = A_{ij}w_c(r_{ij})\mathbf{e}_{ij} + B_{ij}(\rho_i + \rho_j)^s w_d(r_{ij})\mathbf{e}_{ij}. \quad (5)$$

The first term with  $A < 0$  represents the attractive force within a cutoff range  $r_c$ , and the second term with  $B > 0$  is the repulsive force within a cutoff range  $r_d$ . Because a DPD model with a single interaction range cannot maintain a stable interface,<sup>43</sup> the repulsive contribution in Eq. (5) is set to act within a shorter range  $r_d < r_c$  than the soft pair attractive potential. The weight functions are defined as  $w_c(r_{ij}) = 1 - r_{ij}/r_c$  and  $w_d(r_{ij}) = 1 - r_{ij}/r_d$ . The density of each particle is defined as

$$\rho_i = \sum_{j \neq i} w_\rho(r_{ij}), \quad (6)$$

and its weight function  $w_\rho$  is defined as

$$w_\rho = \frac{15}{2\pi r_d^3} \left(1 - \frac{r}{r_d}\right)^2, \quad (7)$$

where  $w_\rho$  vanishes for  $r > r_d$ .

We generalize the local density term  $(\rho_i + \rho_j)$  in Eq. (5) with an exponent  $s$ . When  $s = 1$ , the local density term used in Warren's MDPD system<sup>42</sup> is recovered. The motivation to introduce the tunable exponent is to adjust the Mach number (impact velocity/sound speed). For impacting velocity 1.0 in the DPD system, which is used in this study, the Mach number  $Ma \sim 1/20$ , which is not low-speed impact anymore.<sup>44</sup> One way to lower  $Ma$  is to decrease the impact velocity. In order to maintain the  $We$ , the droplet size should increase, resulting in an exponentially increasing computational cost. Another approach is to increase the sound speed which is related to the compressibility of

media. Even the MDPD liquid is relatively incompressible compared to the highly compressible DPD fluid; its compressibility still needs to be enhanced in this problem. By adding the exponent  $s$  of the local density term, we have a direct way to tune the compressibility of the MDPD fluid. By tuning  $s$  from 1 to 3, we report a seven times increase in the sound speed and a decrease in  $Ma$  from  $\sim 1/20$  to  $\sim 1/130$ . With the exponent  $s$  increasing from 1 to 3, the computational cost still remains in the same order. As a comparison, the computational cost would increase more than 46 000 times by tuning the droplet size. The  $Ma \sim 1/130$  indicates a common low-speed impact and is in the range of most relevant experiments. The following results are all conducted at this  $Ma$ .

## B. Modeling of droplets and substrates

We construct a system consists of a liquid droplet (MDPD particles) and a solid surface (frozen MDPD particles). The simulation box has dimensions  $\{L_x, L_y, L_z\} = \{200, 200, 100\}$ , with periodic boundary conditions imposed on the  $x$  and  $y$  boundaries. We note here that all the properties in DPD simulation are in DPD units, which can be converted to physical units once the scaling relationships are established. The MDPD parameters are as follows:  $A_{ll} = -40$ ,  $B_{ll} = 3$ ,  $A_{ls} = 0$ ,  $B_{ls} = 10$ ,  $r_c = 1.0$ ,  $r_d = 0.75$ ,  $\gamma_{ll} = 8$ ,  $\gamma_{ls} = 8$ , and  $s = 3$ .  $A$  and  $B$  are parameters in Eq. (5), which control the attractive and repulsive force between MDPD particles, respectively.  $r_c$  and  $r_d$  are the cutoff range of attractive and repulsive force in Eq. (5).  $\gamma$  controls the MDPD viscosity. Subscript  $ll$  or  $ls$  indicates the parameter applied to liquid–liquid interaction or liquid–solid interaction.  $s$  is the exponent of local density in Eq. (5). The measured liquid properties are as follows in DPD units: density  $\rho = 5.82$ , dynamic viscosity  $\mu = 7.44$ , surface tension  $\sigma = 4.92$ , and contact angle  $CA \approx 155^\circ$ . The droplet contains 658 503 DPD particles resulting in a radius of 30.0. The default impact velocity  $U_0 = 1.0$ , which leads to  $We = 71.1$ . Other dimensionless numbers are  $Re = 46.9$ , capillary number  $Ca = \mu U_0 / \sigma = 1.52$ , and Ohnesorge number  $Oh = \mu / \sqrt{\rho \sigma D} = 0.18$ . We adopt the boundary condition scheme proposed by Li *et al.*<sup>45</sup> throughout the paper. In this scheme, by introducing an indicator variable of boundary volume fraction for each fluid particle, the boundary of arbitrary-shape object is detected on-the-fly for the moving fluid particles using only the local particle configuration. The scheme has been verified to yield correct no-slip boundary conditions for velocity and generate negligible fluctuations of density and temperature in the vicinity of the wall surface.

Figure 1 is the diagram of the setup. The left half is the DPD particle view, and the right half is the rendered view. Throughout the paper, the radius of the liquid droplet is denoted by  $R$ , the radius of the ring is denoted by  $r$ , and the height of the ring is denoted by  $h$ . All of them are depicted in Fig. 1. The solid substrate is on the  $xy$  plain, and  $z$  is the vertical direction.

All properties in the DPD model are in DPD units, which are non-dimensional. Once the target liquid properties are determined, the scaling relationships can be established. For example, to map the above-mentioned MDPD liquid properties ( $\rho$ ,  $\mu$ , and  $\sigma$ ) to liquid water at room temperature, the explicit DPD scaling relationships are as follows:  $l_{\text{DPD}} = 7.1 \times 10^{-9}$  m,  $t_{\text{DPD}} = 6.2 \times 10^{-23}$  s,  $m_{\text{DPD}} = 6.5 \times 10^{-11}$  kg. Any values in non-dimensional DPD units can be converted to physical properties using these relationships and vice versa. To map to another liquid, like silicon oil, the scaling relationships



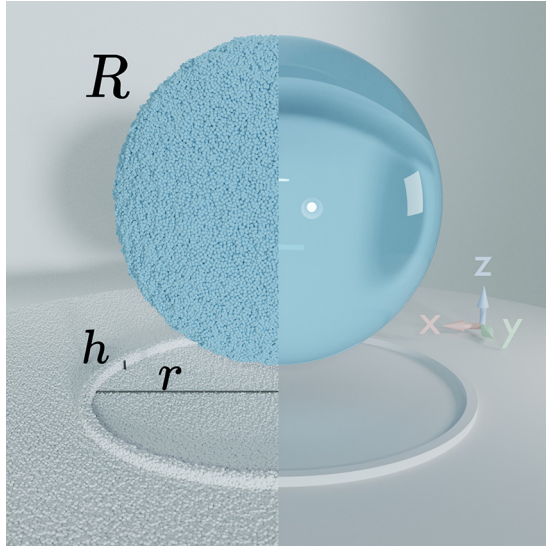


**FIG. 1.** Schematic diagram of the model setup for droplet impacting solid decorated with a ring structure. The left side is the MDPD particle view, and the right side is the rendered view. The droplet is characterized by radius  $R$ , and the ring structure is characterized by radius  $r$  and height  $h$ .

should be derived again, and they will all be different. For generality, we show simulation results in DPD units in Sec. III as most previous DPD works do.

Moreover, we dimensionalize some quantities (length  $l$ , force  $F$ , time  $t$ , and pressure  $P$ ) using the inertial scales (liquid density  $\rho$ , initial impact velocity  $U_0$ , and droplet diameter  $D$ ). We rewrite their dimensionless counterparts as follows:

$$\hat{l} \equiv \frac{l}{D}, \quad \hat{F} \equiv \frac{F}{\rho U_0^2 D}, \quad \hat{t} \equiv \frac{t U_0}{D}, \quad \hat{P} \equiv \frac{P}{\rho U_0^2}. \quad (8)$$

These dimensionless properties are used in Sec. III for comparing with experimental results.

### III. RESULTS AND DISCUSSION

The droplet impacting ring surface and plain surface are comparatively studied. We approach the problem from the following perspective, the different liquid shape evolution, the velocity field, the force profile, the spatiotemporal pressure evolution, the contribution of different solid regions, and the effect of ring radius and height. Through these numerical experiments, we aim to better understand the process of droplet landing on the simple but interesting ring structure.

#### A. The interaction parameter and overrun/ejection phenomenon

To quantitatively evaluate the contact time and contact area, we define the interaction parameter,  $I$ , which is the integral of the liquid-solid contact area over time,<sup>38</sup>

$$I = \int_0^T A(t) dt, \quad (9)$$

where  $A(t)$  is the contact area at time  $t$ , and  $T$  is the overall contact time. We set the  $I$  with a plane surface as the reference  $I_0$ . Then, we could easily evaluate the reduction effect of a new solid surface by comparing  $I$  with  $I_0$ . The  $A(t)$  is measured by counting the liquid particles within the unit length range of solid particles and dividing it by the liquid density. This is an advantage of DPD compared to experiments, which can only infer the contact area indirectly with many difficulties, such as the limitation of view and the distortion from the liquid.

Figure 2 shows the normalized interaction parameter,  $I/I_0$ , vs the normalized ring size,  $r/R$ . The insets are the corresponding slice view snapshots. When  $r$  is smaller than  $R$ , the droplet overruns and spreads horizontally on the plane. We notice the ring hardly has any effect on the spreading and the  $I/I_0$  is around 1.0. Once  $r$  is bigger than  $R$ , the ring redirects the spreading lamella to the air and avoids wetting outside the ring. The  $I$  is dramatically reduced by around 60% in this case. Bigger rings eject the liquid lamella too; however, the  $I$  continues to increase until the ring is bigger than the maximum lamella spreading radius.

In Fig. 2, the  $I/I_0$  shows a sharp transition near  $r/R = 1.1$ . It is concurrent with the transition of two phenomena: overrun and ejection. Next, we will discuss these characteristic phenomena and investigate them from a velocity field aspect.

Figure 3 shows three shape evolution as droplet impacting on a plain and two ring surfaces. Figures 3(a) and 3(b) show the initial state and snapshots as a droplet landing on the plain substrate. Figures 3(c) and 3(d) are the overrun phenomenon on ring substrate. Figure 3(e) and 3(f) are the ejection phenomenon on ring substrate where ring is slightly bigger than that in the overrun case. In order to show the structure of solid substrate clearly, we use the cross section view in all snapshots, which means the front half of the liquid and solid are invisible. All the drops impact the substrate at the same speed ( $v_{\text{DPD}} = 1.0$ ). For better comparison, the snapshots are captured at the same time between different groups.

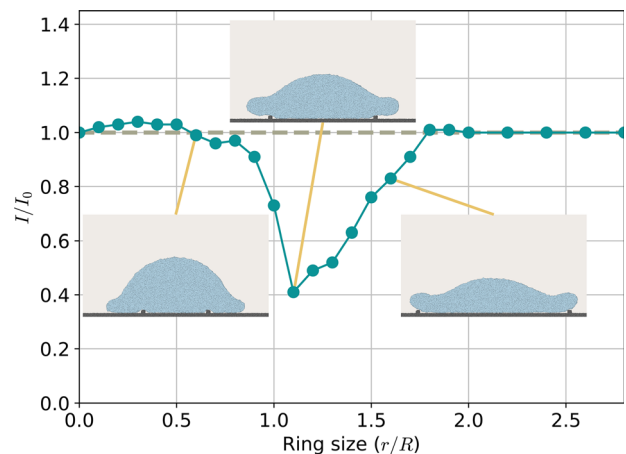


**FIG. 2.** Interaction parameter of an impacting droplet on a surface decorated with a ring structure. The interaction parameter is normalized by that obtained in the reference case of a regular superhydrophobic surface. When the ring is slightly larger than the droplet, the interaction parameter decreases dramatically. The sharp transition is concurrent with the transition of the overrun and ejection phenomena.

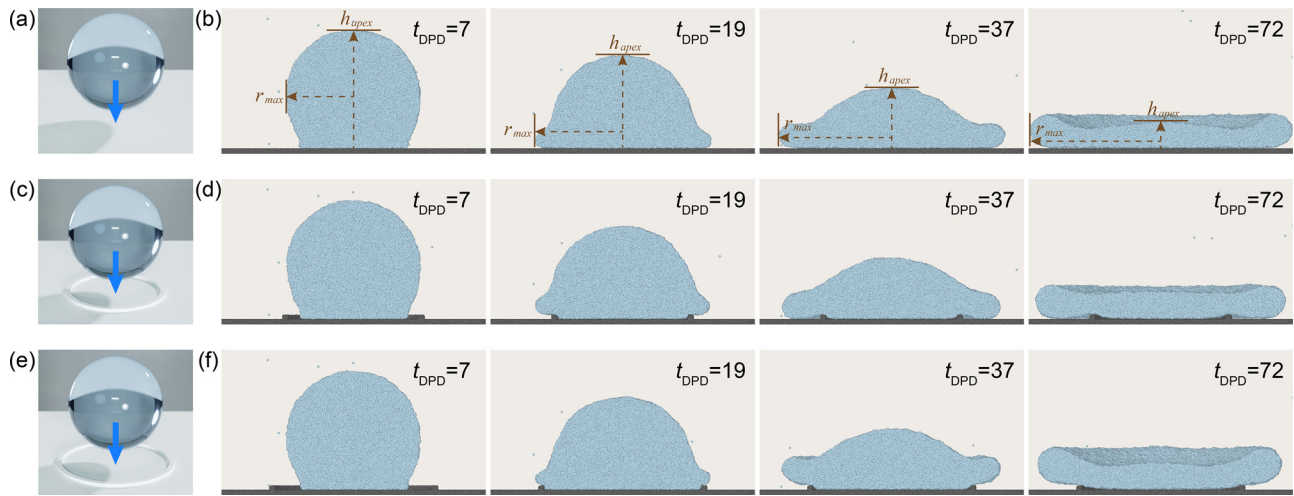


**FIG. 3.** Shape evolution as droplet impacting on different substrates with same speed. (a) Plain surface. (b) The droplet spreads along the plain surface and finally reaches its maximum radius. (c) Ring surface (overrun). (d) The spreading lamella overruns the ring and spreads along the solid. (e) Ring surface (ejection). (f) The spreading lamella is ejected and spreads into the air.

In the initial stage ( $t_{\text{DPD}} = 7$ ), the droplet starts to spread along the solid. All three shapes are the same because the lamella has not reached the ring structure. In the second stage ( $t_{\text{DPD}} = 19$ ), the droplet spreads horizontally on the plain surface; the spreading lamella is redirected by the obstacle and spread into the air on the ring surface. In the third stage ( $t_{\text{DPD}} = 37$ ), the droplet on the plain keeps expanding along the solid; in the overrun case, the downward momentum of the bulk droplet suppresses the flying lamella and the flying lamella returns to spread along the solid; in the ejection case, the upward momentum of the flying lamella is larger than the suppressing downward momentum and the lamella keeps spreading in the air. In the last stage ( $t_{\text{DPD}} = 72$ ), three droplets reach their maximum radius.

We notice the radius in overrun case is smaller compared with that in plain case. This is reasonable because the horizontal spreading is interrupted by the ring and the radial outward momentum is redirected. In the ejection case, the maximum radius is even smaller, as more horizontal momentum is redirected upward. The lamella in the air keeps the solid outside the ring dry from the beginning to the end.

What causes that small difference in ring structure to end up with different droplet phenomena and sharp transition in interaction parameter? In Fig. 4, we further investigate the velocity field. Considering the water bowl is basically rotationally symmetrical, we divide the space into cylindrical bins, each bin has a height of 1.0 and a radial increment of 1.0. We first average the vertical velocity,  $v_z$ , and

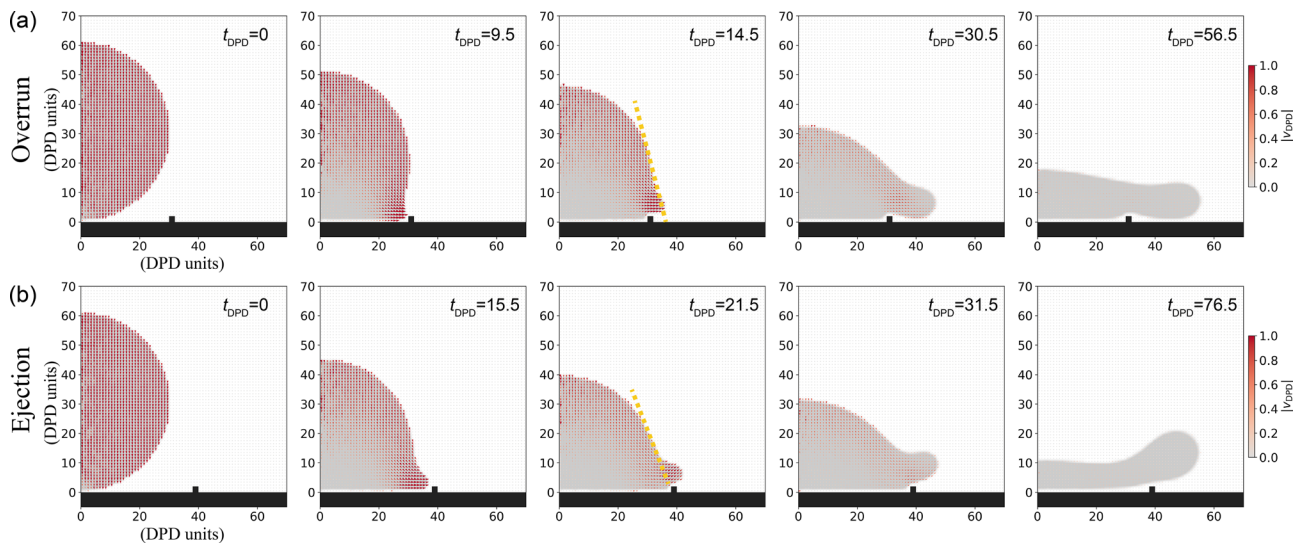


**FIG. 4.** The velocity field of overrun and ejection phenomena. The ring radius is a little larger in the ejection case than that in the overrun case. The yellow line indicates the slope of the free surface, showing where the downward momentum hits.

radial velocity,  $v_r$ , of all the particles in each bin, then time-average 50 snapshots with 0.0005 time step. In Fig. 4, the liquid shape is outlined for clarity by averaging the particle number density in each bin and coloring the space occupied by liquid. The space covered with black represents the solid surface.

Figure 4 shows that the lower part of the droplet starts to decelerate as soon as it contacts the solid. Meanwhile, the upper part of the droplet remains the initial impacting speed as the impact has not happened. The trajectory of the droplet's apex shows more evidence [Fig. 5(a)] as we will discuss later. After the impact, the liquid near the contact line starts to spread outward, and the traveling speed is much faster than the initial speed.

In the middle stage, the centroid of mass keeps descending. The movement near the free surface is much faster than that near the centerline. In the overrun case, the huge descending momentum near the free surface finally lands on the flying lamella and suppresses the lamella back to the substrate. In the ejection case, most of the descending momentum lands inside the ring. Those liquids will be redirected by the ring and gain upward momentum later. In the competition between the upward lamella and the downward droplet free surface, the upward lamella prevails until the end of spreading.

## B. The transient force profile of impact

In this section, we investigate the time-varying impacting force. Although the force consists of two parts: the vertical force and the horizontal force, we refer to the vertical force throughout the paper, unless otherwise stated. In the DPD simulation, the force at time  $t$  is calculated as follows: first, compute the interaction force of each pair which includes one solid particle and one liquid particle (this is not extra burden for a DPD simulation); next, calculate the summation across the system; finally, average across a time window (50 snapshots with a time step of 0.0005).

Before we start to investigate the impacting force on ring substrate, we first validate our model on a plain substrate where plentiful

experimental data exist. These data cover different liquid materials, various droplet sizes, and a wide range of impacting velocities. Fortunately, some similarities in the dimensionless form of the impacting force have been reported.<sup>10–12</sup>

Figure 5 shows our simulation results along with the corresponding theoretical and experimental reference. Figure 5(b) is the impacting force as a function of time. The snapshots of the droplet are shown next to the curve. The blue thin lines are the raw DPD force with noticeable noise. To reduce the noise, we conduct five separate simulations and plot the ensemble average with the orange color. The force profile displays a sharp increase upon impact at  $\hat{t} = 0$ , reaches a maximum at  $\hat{t} = \hat{t}_{\max}$ , and then slowly decays to zero in  $\hat{t} \sim 1.6$ . In the regime of initial impact before  $\hat{t}_{\max}$ , the impact of liquid drops is dominated by inertia. Strong pressure gradients develop near the solid surface, which drives a rapid deformation of the droplet and redirects the flow from the vertical to the horizontal direction. The self-similar pressure and velocity fields are reported by many researchers.<sup>10,12</sup> From a theoretical point of view, the self-similar length scale of the self-similar fields is given by  $\sqrt{U_0 D t}$ . The predicted self-similar pressure gives an instantaneous impact force following

$$F(t) = \frac{3}{2} \sqrt{6} \rho U_0^{5/2} D^{3/2} t^{1/2}. \quad (10)$$

Its dimensionless form can be written as

$$\hat{F}(\hat{t}) = \frac{3}{2} \sqrt{6} \hat{t}^{1/2}. \quad (11)$$

As for experiments, Gordillo *et al.*<sup>10</sup> have done systematic research on the dynamics of droplet impacting on solid surfaces under various conditions and concluded that the force follows the form

$$\hat{F}(\hat{t}) = \alpha \hat{t}^\beta, \quad (12)$$

where  $\alpha \approx 4.1$  and  $\beta = 0.5$  for  $Re = 46.9$  which is our case.

The above estimation only covers the initial stage of impact. Mitchell *et al.*<sup>11</sup> construct a single, accurate model equation for the

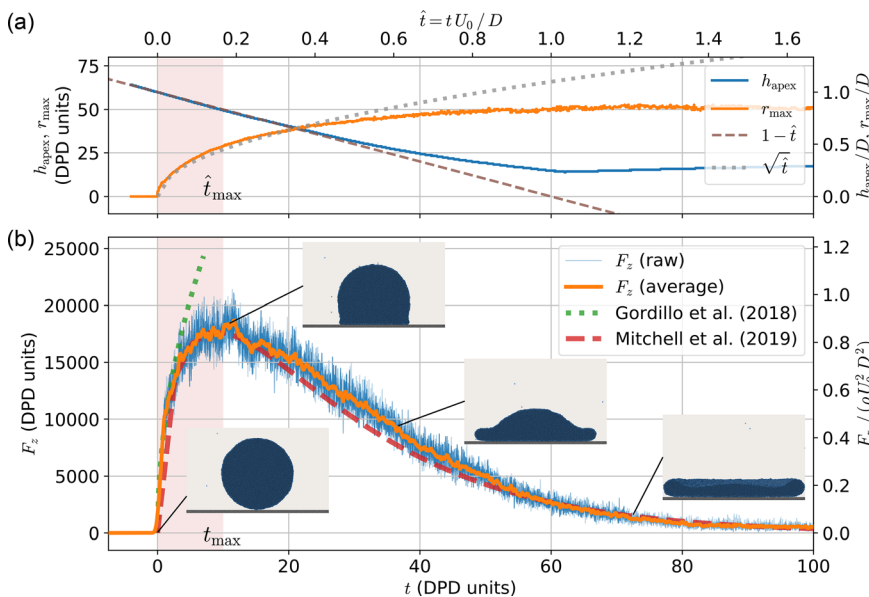


**FIG. 5.** A droplet impacts on a plain surface. (a) Temporal evolution of the shape of the impacting drop, quantified by the apex position of the droplet  $h_{\text{apex}}(t)$ , and the radius of the spreading contact line,  $r_{\text{max}}(t)$ . The linear dashed line has a slope of  $-U$  (or  $-1$  in the dimensionless form), indicating the trajectory of the droplet as if the impact never happened. The dotted line indicates the  $\sqrt{t}$  scaling of  $r_{\text{max}}$ . (b) Temporal evolution of the impact force,  $F_z(t)$ . Five separate simulations are conducted, and the raw data and ensemble average are both plotted. The green dotted line is the prediction of the self-similar theory of initial impacts from Philipp *et al.*<sup>12</sup> The red dashed line is the prediction model proposed by Mitchell *et al.*<sup>11</sup> which can capture the full force evolution including the initial impacts and the exponential decay thereafter.



force profiles, incorporating the  $\sqrt{t}$  short-time behavior and the  $e^{-t}$  long-time exponential post-peak decay behavior. The dimensionless form of the equation is

$$\hat{F}(\hat{t}) = \sqrt{\frac{1000\pi\hat{t}}{243}} e^{-10\hat{t}/3}. \quad (13)$$

Comparing the initial region with Eq. (12) and the entire force profile with Eq. (13), we find our results generally agree with the previous studies. The dimensionless peak force,  $\hat{F}_{\max}$ , and dimensionless peak time,  $\hat{t}_{\max}$ , are two essential features of the force profile. The measured values from our simulation are  $\hat{F}_{\max} \approx 0.95$  and  $\hat{t}_{\max} \approx 0.17$ , which match the experimental data quite well.<sup>10</sup>

Previous studies also claim that the existence of upward expanding self-similar pressure fields during the initial impact, from both simulations<sup>12</sup> and experiments.<sup>10</sup> Before the upper bound of the high-pressure region reaches the top surface of the liquid drop, the motion of the droplet apex should remain unchanged as if the droplet had not experienced any impact. In Fig. 5(a), the apex of the drop (see definition in Fig. 3),  $h_{\text{apex}}$ , keeps descending at the initial speed  $U_0$  without any perceptible changes. Here, our simulation results provide further evidence that this unusual phenomenon arises from the finite

propagation speed of the high-pressure fields, and this is the first time MDPD simulations confirm this phenomenon. Since the pressure field may touch the upper surface of the droplet before reaching the apex, the impact force may start to deviate from the prediction of the initial impact self-similar theory, when  $h_{\text{apex}}$  is still outside the self-similar region and maintains its constant-velocity descent. This phenomenon is reported in experimental studies<sup>10</sup> and also observed in our MDPD simulation. In Fig. 5, the impact force reaches its maximum and begins to decrease before the apex of the droplet showing any clear deviation from  $U_0$ . The  $1 - \hat{t}$  dashed line provides a guideline for descending with constant  $U_0$  in dimensionless form.

During the initial impact, the deformation of the droplet is limited within the self-similar high-pressure region. It has been suggested that this high-pressure region occupies a volume with the same radius as the contact area between the droplet and the solid surface. Indeed, previous studies and our simulations have all confirmed that the radius of the spreading contact line increases as  $r_{\max} \sim \sqrt{t}$  at short times during initial impact [Fig. 5(a)].

After validating our MDPD model on a plain surface, we explore the kinematics and dynamics of the impact on a ring surface. We show results of an overrun and an ejection cases in Fig. 6. The impact velocity is 1.0 and the height of the ring is  $h/R = 0.067$ . The only

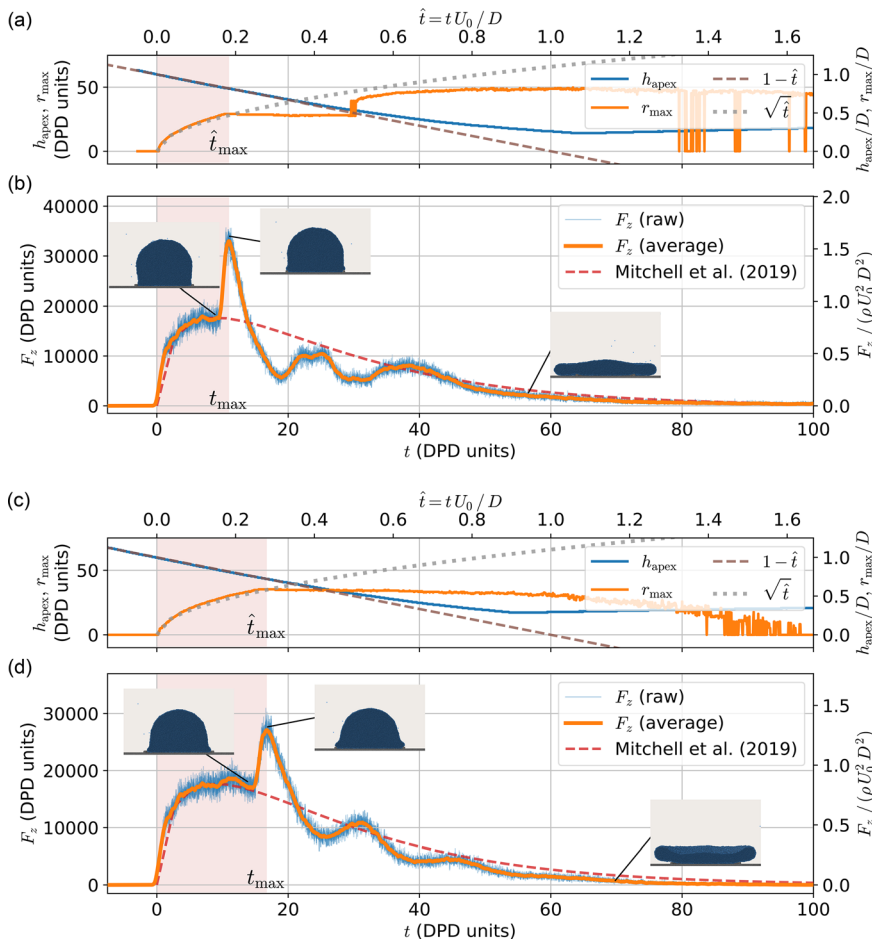


**FIG. 6.** A droplet impacts on a ring surface. (a) and (b) Overrun. The ring structure has a radius of  $r/R = 1.0$ . The  $r_{\max}$  reflects the overrun process with a sudden jump at  $\hat{t} = 0.47$ . After the lamella hits the ring, the  $F_z$  increases sharply and almost doubles. Then, the force decreases rapidly and experiences some fluctuations, finally, it overlaps with the prediction of Mitchell which represents the force profile on a plain substrate. (c) and (d) Ejection. The ring structure has a radius  $r/R = 1.2$ . The plateau of  $r_{\max}$  reveals the lamella never reaches the outer solid. Compared to the overrun case, the peak  $F_z$  is weaker and appears later. It is worth noting that the contact area is totally different when the force reduces to zero. In overrun case, the droplet is widely spread on solid, while in ejection case, the droplet has a liftoff.



input difference between the two cases is the ring radius ( $r/R = 1.0$  for overrun and  $r/R = 1.2$  for ejection).

Figures 6(a) and 6(b) are the overrun case. In Fig. 6(a), the  $h_{\text{apex}}$  is similar to that of a plain case.  $r_{\text{max}}$  stops growing at  $\hat{t} = 0.19$  since the ring blocks the lamella. Later,  $r_{\text{max}}$  shows a sudden jump, because the lamella overruns the ring and touches the ground again, approximately at  $\hat{t} = 0.48$ . The  $r_{\text{max}}$  increases gradually thereafter and shows some instability in the late stage. The instability of  $r_{\text{max}}$  is due to the detaching of the droplet and the definition of  $r_{\text{max}}$ , which is the max radius of the contacting liquid particles.

In Fig. 6(b), the force profile is the same as Fig. 5 at the beginning. Then the force increases sharply and is almost doubled. It subsequently experiences a rapid decrease ensued by some fluctuations and finally overlaps with the prediction of Mitchell *et al.*<sup>11</sup> which represents the force profile on a plain surface. The time at which force returns to zero is only slightly ahead of that on a plain.

Figures 6(c) and 6(d) are the overrun case. In Fig. 6(c),  $r_{\text{max}}$  stops growing at  $\hat{t} = 0.27$  since lamella is blocked by the ring. This confinement effect persists and the  $r_{\text{max}}$  gradually shrinks in the late stage.

In Fig. 6(b), the force reaches the peak later compared to the overrun case due to the bigger ring. The peak force is also weaker because the liquid velocity is slower when it reaches the ring structure. After several fluctuations, the force returns to zero, and the time is slightly earlier than that in the overrun or plain case. It is worth noting that the contact

area is quite different when force reduces to zero in different cases. For example, at  $t = 100$ , the droplet is in wide contact with solid in the overrun and plain cases, but liftoff in the ejection case.

### C. Spatiotemporal evolution of pressure on substrate

In this section, we investigate the spatiotemporal evolution of interface pressure and compare the results of plain surfaces with ring surfaces. Due to the rotational symmetry, we divide the interface into concentric rings, each ring has a thickness of 0.5 in the radial direction. The results are shown in Fig. 7. The time ( $x$  axis) and radial distance ( $y$  axis) are both presented in their dimensionless form. The pressure value is displayed by color.

First, we check the heatmap of pressure on the plain surface [Fig. 7(a)]. The high-pressure region appears at the center (near I) where the droplet first contacts the solid. Then, it moves along the contact line (near II) rather than stays at the center. This is consistent with the findings in Philippi *et al.*<sup>12</sup> As the droplet spreads, the pressure near the contact line is decaying faster (near III) compared to that near the center (near IV). We also note that the data near the center (near IV) is noisier, it is because the rings near the center are smaller and have fewer DPD particles to average.

Figure 7(b) is the overrun case on a ring surface. Compared to the plain case, the biggest difference is the huge and sharp force

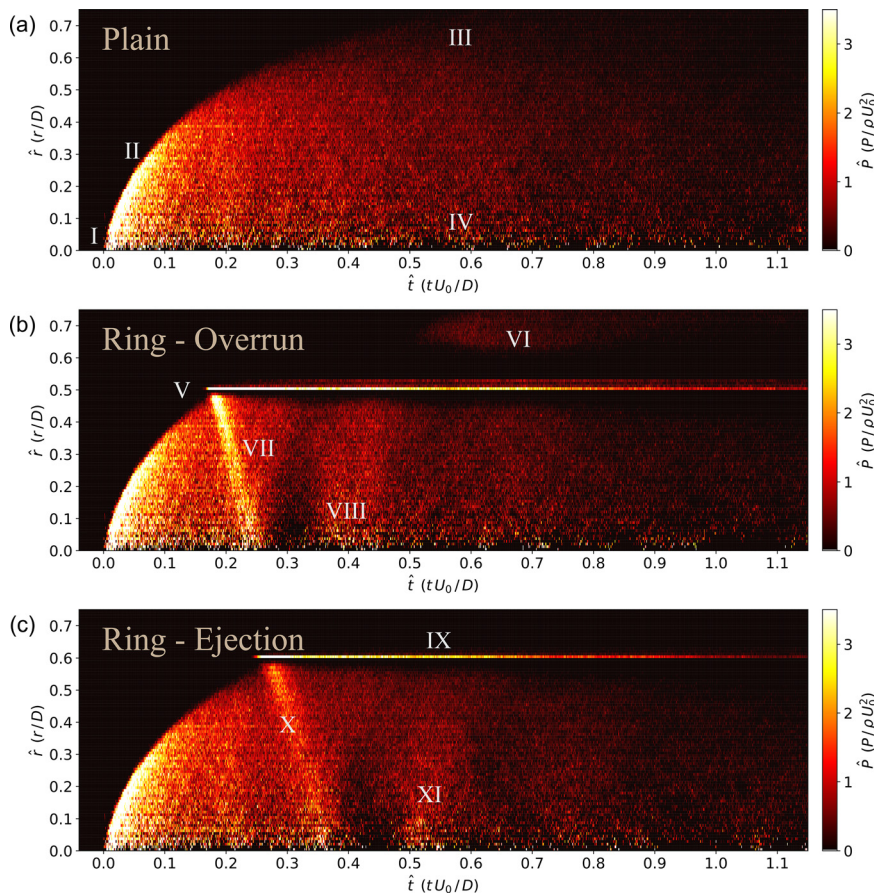


**FIG. 7.** Radical distribution of dimensionless pressure as a function of time. (a) Plain. The high pressure appears at the center (near I) where the droplet first contacts the solid and then moves along the contact line (near II). As droplet spreads, the pressure near the contact line (near III) decays faster than that near the center (near IV). (b) Ring-overrun. Compared to the plain case, the biggest difference is the highlight high-pressure belt at the ring position (near V). The spreading of the pressure field is truncated by the ring, and the solid outside the ring provides trivial upward force (near VI). Another difference is the pressure waves propagating from ring to center and backward (near VII and VIII). (c) Ring-ejection. Similar to ring-overrun, the pressure outside the ring is totally zero, and the high-pressure belt (near IX) is weaker.

appears at the ring location (near V). The expansion of the pressure field is truncated by the ring, but some liquid still touches the outside later (near VI). From the plot, we can tell the impact outside the ring is very soft and blur. Moreover, we observe a clear high-pressure wave (near VII) which is not presented in plain case. The high pressure arises when the spreading lamella first hits the ring. Then, it propagates backward to the center at a constant speed. Instead of bouncing back immediately, the second high-pressure wave (near VIII) arises with some time lap. These waves damp out after  $\hat{t} = 0.7$ .

The results of the ejection case are shown in Fig. 7(c). It is similar to the overrun case. One difference is the location of the high-pressure belt (near IX), which is determined by the location of the ring. Another difference is that there is no pressure detected beyond  $\hat{r} = 0.63$ . The high-pressure wave also exists (near X), but the intensity is lower than that in the overrun case. The slope of the wave (wave speed) is the same as that in Fig. 7(b), and similarly, a second and weaker wave (near XI) is observed.

#### D. The role of ring

The difference in force profile between the plain surface and ring surface is obvious [Figs. 5(b), 6(b), and 6(d)]. How does a relatively small ring ( $h/D = 0.03$ ) cause such a big difference? In this section, we split the ring-decorated substrate into three parts: the ring (solid above the plain), the inner (plain inside the ring), and the outer (plain outside the ring). See Fig. 8(a) for the example of the three regions.

The dark green, medium green, and light green indicate the inner, ring, and outer region, respectively, and the blue particles are liquid spreading toward the ring. Similar to the previous approach, the  $F_z$  provided by different parts ( $F_{\text{ring}}$ ,  $F_{\text{inner}}$ ,  $F_{\text{outer}}$ ) are computed by the summation of the forces between liquid particles and corresponding solid particles in different regions. All the solid structures have a thickness of 2.0, which is larger than the DPD cutoff distance 1.0 to eliminate the solid thickness effect.

Figure 8(b) is the force profiles of the three parts. Both ejection and overrun cases are presented. The solid lines are the total force from the solid, including the ring, inner, and outer. The dashed and dotted lines are the separate force from the three parts. The force on the plain surface is also presented for reference.

Even the force spike is caused by the presence of ring structure, the results indicate that the ring itself contributes a small amount of  $F_z$  in both overrun and ejection cases. Instead, the inner solid part makes the main contribution, which is almost decisive for the force profile.

The  $F_{\text{ring}}$  arises when lamella hit the ring. It is rather stable and decays very slowly compared to  $F_{\text{inner}}$ . What's more, the  $F_{\text{ring}}$  profile for both overrun and ejection cases are quite similar.

The  $F_{\text{outer}}$  is the weakest in the three portions. For overrun case, it start at  $t_{\text{DPD}} = 30$ , with a soft start compared to that of  $F_{\text{ring}}$ . For the ejection case, it remains 0 all the time. Considering their magnitude, both  $F_{\text{outer}}$  and  $F_{\text{ring}}$  are trivial in the total force.

From the results, we conclude that the ring's role is not providing  $F_z$  by itself, but redirecting the horizontal spreading liquid to the

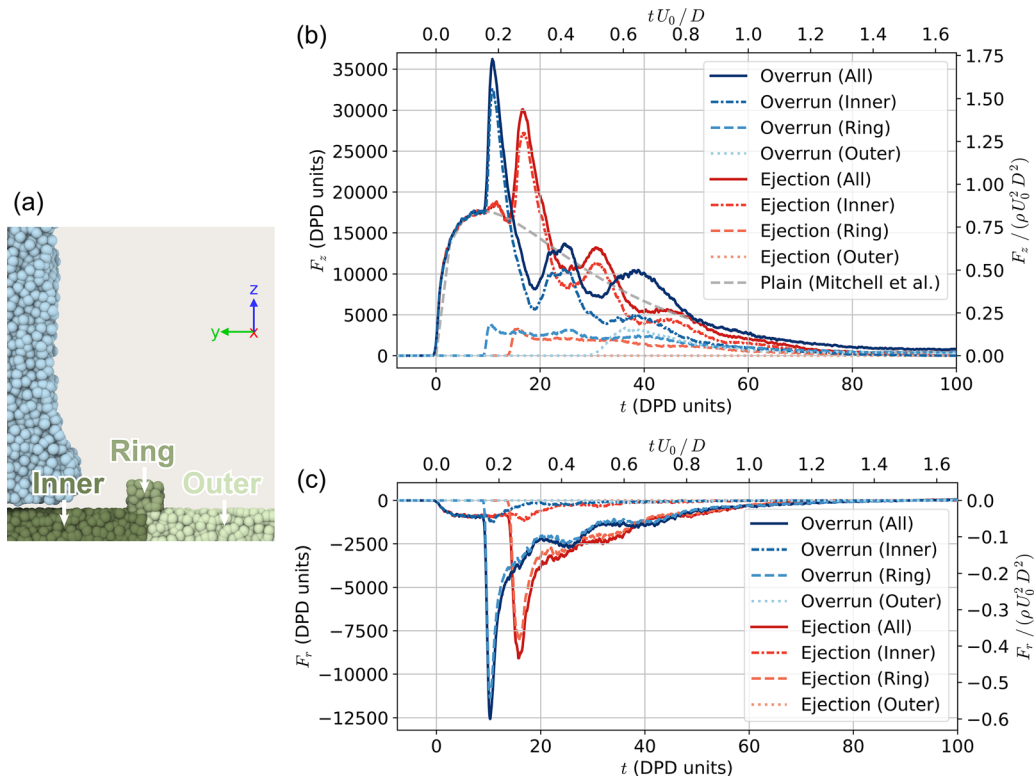


**FIG. 8.** (a) Definition of the ring, inner, and outer regions. (b) The total vertical force ( $F_z$ ) and its three components (ring, inner, and outer). The results show that the force from the inner is the majority. The force from the ring is relatively small. (c) The horizontal radial force ( $F_r$ ) and its three components.

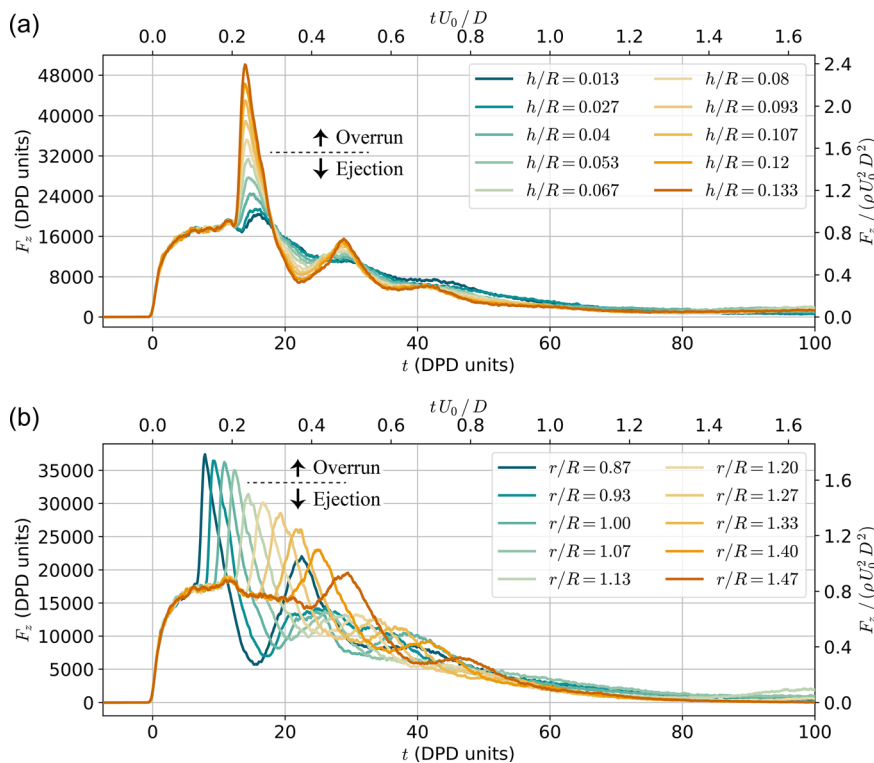


**FIG. 9.** The effect of ring height  $h$  and ring radius  $r$  on the impacting force. There is no obvious gap in force profiles between overrun and ejection phenomena, unlike the interaction parameter.

vertical direction. A portion of the liquid goes upward, and the rest goes downward. The downward stream increases the pressure on the inner solid part and results in growing  $F_z$ .

Additionally, we show the horizontal radial force ( $F_r$ ) results in Fig. 8(c). The outward direction is defined as the positive direction. We notice the relative increment induced by the ring is much larger than that in  $F_z$ . In overrun case, the  $F_r$  increases almost tenfold after hitting the ring. Different from the  $F_z$  analysis where the inner part plays the major role, here the ring is the dominant part.

### E. The effect of ring height and ring radius

In this section, we investigate the effect of ring height  $h$  and ring radius  $r$  on  $F_z$ .

Figure 9(a) is the results of the  $h$  effect. The tested  $h$  ranges from  $h/R = 0.0$  to  $h/R = 0.133$ , while  $r/R = 1.133$  keeps constant. Same as previous figures, the DPD time and dimensionless time are both labeled, so are the DPD force and dimensionless force.

The variation of  $h$  seems to only affect the peak force but not the  $t_{\max}$ , the time instant associated with the peak force. The invariance of  $t_{\max}$  is reasonable because the ring radius is the same in all cases. The main difference for different  $h$  is the magnitude of peak force, which increases monotonously as  $h$  increases. In the decaying regime, a higher peak force is always followed by stronger oscillation and faster decay.

From a morphology perspective,  $h/R \approx 0.07$  is the critical value for overrun and ejection phenomena. Even though the droplet shapes

are quite different, their impact force profiles are changing rather continually, not showing a sharp transition as the interaction parameter does.

Figure 9(b) is the result of  $r$  effect. The tested  $r$  ranges from  $r/R = 0.87$  to  $r/R = 1.33$ , while  $h/R = 0.067$  keeps constant. Compared to the effect of  $h$ , the effect of  $r$  is more complex. It affects both the peak force and the  $t_{\max}$  at the same time. As  $r$  increases, the peak force decreases monotonously. We believe the main factor affecting the peak force is the speed of lamella when hitting the ring, considering other factors, such as the ring height, the initial droplet speed, and the liquid density, are invariant in these cases. As for the  $t_{\max}$ , it increases monotonously as  $r$  increases. The  $t_{\max}$  basically denotes the time lamella reaches the ring.

The time of  $F_z$  decaying to zero is slightly different in different cases. Generally, the case with lower peak force decays faster. This is opposite to the  $h$  effect, where a higher peak force case decays faster.

The critical value for overrun and ejection phenomena is  $r/R \approx 1.10$ . It is marked near the peak force. There is a modest gap between the overrun and ejection force profiles. Overall, the force profiles change continuously, in contrast to the sharp transition of interaction parameter.

### IV. CONCLUSIONS

In this work, we use the MDPD method to investigate the droplet impacting on a ring surface. A tunable exponent in MDPD conservative force is introduced to adjust the  $Ma$  of the system. The main findings are summarized as follows:



- The impacting force on a plain surface computed by our MDPD model is validated with experimental data from the literature in dimensionless form.
- The force profile of overrun phenomenon on ring surface has a higher peak force and a shorter  $t_{\max}$ ; the force profile of ejection phenomenon shows a lower peak force and a longer  $t_{\max}$ . Both peak forces are greater than that on a plain surface.
- The pressure field on the fluid–solid interface show that in the initial stage, the high-pressure region moves with the contact line; after the lamella hits the ring, a high-pressure wave emerges and propagates from ring to center.
- The ring structure does not directly provide the rapid and massive upward momentum to the droplet but induces the inner substrate to do so.
- Unlike the interaction parameter which shows a sharp transition, the impacting force profiles change rather continuously as a function of ring radius or height.

## ACKNOWLEDGMENTS

The authors acknowledge the financial support from the National Natural Science Foundation of China (Nos. 12002242, 11872283, and 11702196), the Fundamental Research Funds for the Central Universities (No. 22120190207), and the National Key Research and Development Program of China (No. 2020YFB0311500).

## AUTHOR DECLARATIONS

### Conflict of Interest

The authors have no conflicts to disclose.

## DATA AVAILABILITY

The data that support the findings of this study are available from the corresponding author upon reasonable request.

## REFERENCES

- <sup>1</sup>M. J. Römkens, K. Helming, and S. Prasad, “Soil erosion under different rainfall intensities, surface roughness, and soil water regimes,” *Catena* **46**, 103–123 (2002).
- <sup>2</sup>A. K. Dickerson, P. G. Shankles, N. M. Madhavan, and D. L. Hu, “Mosquitoes survive raindrop collisions by virtue of their low mass,” *Proc. Natl. Acad. Sci.* **109**, 9822–9827 (2012).
- <sup>3</sup>S. Gart, J. E. Mates, C. M. Megaridis, and S. Jung, “Droplet impacting a cantilever: A leaf-raindrop system,” *Phys. Rev. Appl.* **3**, 044019 (2015).
- <sup>4</sup>J. R. Castrejón-Pita, G. D. Martin, S. D. Hoath, and I. M. Hutchings, “A simple large-scale droplet generator for studies of inkjet printing,” *Rev. Sci. Instrum.* **79**, 075108 (2008).
- <sup>5</sup>V. Bergeron, D. Bonn, J. Y. Martin, and L. Vovelle, “Controlling droplet deposition with polymer additives,” *Nature* **405**, 772–775 (2000).
- <sup>6</sup>B. Amirzadeh, A. Louhghalam, M. Raessi, and M. Tootkaboni, “A computational framework for the analysis of rain-induced erosion in wind turbine blades, part II: Drop impact-induced stresses and blade coating fatigue life,” *J. Wind Eng. Ind. Aerodyn.* **163**, 44–54 (2017).
- <sup>7</sup>A. A. Fyall, “Practical aspects of rain erosion of aircraft and missiles,” *Philos. Trans. R. Soc. London, Ser. A* **260**, 161–167 (1966).
- <sup>8</sup>J. Li, B. Zhang, P. Guo, and Q. Lv, “Impact force of a low speed water droplet colliding on a solid surface,” *J. Appl. Phys.* **116**, 214903 (2014).
- <sup>9</sup>B. Zhang, J. Li, P. Guo, and Q. Lv, “Experimental studies on the effect of Reynolds and Weber numbers on the impact forces of low-speed droplets colliding with a solid surface,” *Exp. Fluids* **58**, 125 (2017).
- <sup>10</sup>L. Gordillo, T. Sun, and X. Cheng, “Dynamics of drop impact on solid surfaces: Evolution of impact force and self-similar spreading,” *J. Fluid Mech.* **840**, 190–214 (2018).
- <sup>11</sup>B. R. Mitchell, J. C. Klewicki, Y. P. Korkolis, and B. L. Kinsey, “The transient force profile of low-speed droplet impact: Measurements and model,” *J. Fluid Mech.* **867**, 300–322 (2019).
- <sup>12</sup>J. Philippi, P. Lagrée, and A. Antkowiak, “Drop impact on a solid surface: Short-time self-similarity,” *J. Fluid Mech.* **795**, 96–135 (2016).
- <sup>13</sup>I. V. Roisman, E. Berberović, and C. Tropea, “Inertia dominated drop collisions. I. On the universal flow in the lamella,” *Phys. Fluids* **21**, 052103 (2009).
- <sup>14</sup>Y. Yu and C. Hopkins, “Experimental determination of forces applied by liquid water drops at high drop velocities impacting a glass plate with and without a shallow water layer using wavelet deconvolution,” *Exp. Fluids* **59**, 84 (2018).
- <sup>15</sup>A. S. Grinspan and R. Gnanamoorthy, “Impact force of low velocity liquid droplets measured using piezoelectric PVDF film,” *Colloids Surf. A* **356**, 162–168 (2010).
- <sup>16</sup>D. Soto, A. B. De Larivière, X. Boutillon, C. Clanet, and D. Quéré, “The force of impacting rain,” *Soft Matter* **10**, 4929–4934 (2014).
- <sup>17</sup>B. R. Mitchell, A. Nassiri, M. R. Locke, J. C. Klewicki, Y. P. Korkolis, and B. L. Kinsey, “Experimental and numerical framework for study of low velocity water droplet impact dynamics,” in *International Manufacturing Science and Engineering Conference* (American Society of Mechanical Engineers, 2016), Vol. 49897, p. V001T02A047.
- <sup>18</sup>J. Eggers, M. A. Fontelos, C. Josserand, and S. Zaleski, “Drop dynamics after impact on a solid wall: Theory and simulations,” *Phys. Fluids* **22**, 062101 (2010).
- <sup>19</sup>D. Wang, D. Tan, and N. Phan-Thien, “A lattice Boltzmann method for simulating viscoelastic drops,” *Phys. Fluids* **31**, 073101 (2019).
- <sup>20</sup>M. Arienti, W. Pan, X. Li, and G. E. Karniadakis, “Many-body dissipative particle dynamics simulation of liquid/vapor and liquid/solid interactions,” *J. Chem. Phys.* **134**, 204114 (2011).
- <sup>21</sup>J. Zhao, S. Chen, K. Zhang, and Y. Liu, “A review of many-body dissipative particle dynamics (MDPD): Theoretical models and its applications,” *Phys. Fluids* **33**, 112002 (2021).
- <sup>22</sup>L. Lu, Z. Li, H. Li, X. Li, P. G. Vekilov, and G. E. Karniadakis, “Quantitative prediction of erythrocyte sickling for the development of advanced sickle cell therapies,” *Sci. Adv.* **5**, eaax3905 (2019).
- <sup>23</sup>L. Xiao, C. Lin, S. Chen, Y. Liu, B. Fu, and W. Yan, “Effects of red blood cell aggregation on the blood flow in a symmetrical stenosed microvessel,” *Biomech. Model. Mechanobiol.* **19**, 159–171 (2020).
- <sup>24</sup>X. Qi, S. Wang, S. Ma, K. Han, and X. Li, “Quantitative prediction of flow dynamics and mechanical retention of surface-altered red blood cells through a splenic slit,” *Phys. Fluids* **33**, 051902 (2021).
- <sup>25</sup>Z. Li, G. Hu, Z. Wang, Y. Ma, and Z. Zhou, “Three dimensional flow structures in a moving droplet on substrate: A dissipative particle dynamics study,” *Phys. Fluids* **25**, 072103 (2013).
- <sup>26</sup>C. Lin, Z. Li, L. Lu, S. Cai, M. Maxey, and G. E. Karniadakis, “Operator learning for predicting multiscale bubble growth dynamics,” *J. Chem. Phys.* **154**, 104118 (2021).
- <sup>27</sup>S. Chen, N. Phan-Thien, X. Fan, and B. C. Khoo, “Dissipative particle dynamics simulation of polymer drops in a periodic shear flow,” *J. Non-Newtonian Fluid Mech.* **118**, 65–81 (2004).
- <sup>28</sup>X. Li, Y. Tang, H. Liang, and G. E. Karniadakis, “Large-scale dissipative particle dynamics simulations of self-assembled amphiphilic systems,” *Chem. Commun.* **50**, 8306–8308 (2014).
- <sup>29</sup>C. Lin, L. Yang, F. Chen, S. Chen, and H. Yin, “A dissipative particle dynamics and discrete element method coupled model for particle interactions in sedimentation toward the fabrication of a functionally graded material,” *Colloids Surf. A* **604**, 125326 (2020).
- <sup>30</sup>C. Lin, M. Maxey, Z. Li, and G. E. Karniadakis, “A seamless multiscale operator neural network for inferring bubble dynamics,” *J. Fluid Mech.* **929**, A18 (2021).
- <sup>31</sup>C. Lin, S. Chen, L. Xiao, and Y. Liu, “Tuning drop motion by chemical chessboard-patterned surfaces: A many-body dissipative particle dynamics study,” *Langmuir* **34**, 2708–2715 (2018).
- <sup>32</sup>K. Zhang, Z. Li, and S. Chen, “Analytical prediction of electrowetting-induced jumping motion for droplets on hydrophobic substrates,” *Phys. Fluids* **31**, 081703 (2019).



- <sup>33</sup>Y. Wang, J. Zhao, D. Zhang, M. Jian, H. Liu, and X. Zhang, “Droplet sliding: The numerical observation of multiple contact angle hysteresis,” *Langmuir* **35**, 9970–9978 (2019).
- <sup>34</sup>H. Chen, Q. Nie, and H. Fang, “Many-body dissipative particle dynamics simulation of Newtonian and non-Newtonian nanodroplets spreading upon flat and textured substrates,” *Appl. Surf. Sci.* **519**, 146250 (2020).
- <sup>35</sup>A. L. Yarin, “Drop impact dynamics: Splashing, spreading, receding, bouncing...,” *Annu. Rev. Fluid Mech.* **38**, 159–192 (2006).
- <sup>36</sup>C. Josserand and S. T. Thoroddsen, “Drop impact on a solid surface,” *Annu. Rev. Fluid Mech.* **48**, 365–391 (2016).
- <sup>37</sup>H. Girard, D. Soto, and K. K. Varanasi, “Waterbowls: Reducing impacting droplet interactions by momentum redirection,” *ACS Nano* **13**, 7729–7735 (2019).
- <sup>38</sup>C. Lin, K. Zhang, X. Chen, L. Xiao, S. Chen, J. Zhu, and T. Zou, “Reducing droplet contact time and area by craterlike surface structure,” *Phys. Rev. Fluid* **6**, 083602 (2021).
- <sup>39</sup>N. Phan-Thien, N. Mai-Duy, and T. Y. N. Nguyen, “A note on dissipative particle dynamics (DPD) modelling of simple fluids,” *Comput. Fluids* **176**, 97–108 (2018).
- <sup>40</sup>R. D. Groot and P. B. Warren, “Dissipative particle dynamics: Bridging the gap between atomistic and mesoscopic simulation,” *J. Chem. Phys.* **107**, 4423–4435 (1997).
- <sup>41</sup>P. Español and P. Warren, “Statistical mechanics of dissipative particle dynamics,” *Europhys. Lett.* **30**, 191 (1995).
- <sup>42</sup>P. B. Warren, “Vapor-liquid coexistence in many-body dissipative particle dynamics,” *Phys. Rev. E* **68**, 066702 (2003).
- <sup>43</sup>I. Pagonabarraga and D. Frenkel, “Dissipative particle dynamics for interacting systems,” *J. Chem. Phys.* **115**, 5015–5026 (2001).
- <sup>44</sup>Q. Zhou, N. Li, X. Chen, T. Xu, S. Hui, and D. Zhang, “Analysis of water drop erosion on turbine blades based on a nonlinear liquid–solid impact model,” *Int. J. Impact Eng.* **36**, 1156–1171 (2009).
- <sup>45</sup>Z. Li, X. Bian, Y. Tang, and G. E. Karniadakis, “A dissipative particle dynamics method for arbitrarily complex geometries,” *J. Comput. Phys.* **355**, 534–547 (2018).